Erosion and Deposition around Porous Engineered Log Jams: Flume Experiments and Improved Predictive Formulas

Seyedeh Azadeh Mousavi Darzikolaei, S.M.ASCE[1];
Joanna Crowe Curran, Ph.D., M.ASCE[2]; and Xiaofeng Liu, Ph.D., M.ASCE[3]

Abstract: Wood reintroduction into rivers, such as the construction of engineered log jams (ELJs), is increasingly popular in river restoration. ELJs are widely used because they mimic natural hydraulics and are relatively easy to construct. One key characteristic of ELJs is their porosity and resulting leaky nature. Based upon previous work, this study further examines the effects of ELJ porosity on flow and sediment transport. Flume experiments were performed over a wide range of porosity values and two ELJ placements (center and side of channel). Detailed flow and scour were measured and analyzed. To better quantify the porous nature of ELJs, two porosity definitions were proposed: the surface porosity and the volumetric porosity. Based on the two porosity definitions, a general formula for equilibrium scour depth has been developed, which captures the trend and reduces scatter in the data. The formulas were verified with data from a real river restoration project. The temporal evolution of scour depth was further analyzed based on a scaling analysis and a saturation growth curve was proposed.
DOI: 10.1061/JHEND8.HYENG-13983.

Introduction and Literature Review

Overview

Human activities have significantly altered the physical and biological functionalities of rivers and streams on Earth (Bernhardt et al. 2005; Vitousek et al. 1997). Actions such as removing trees and debris from rivers for flood control (Harmon et al. 1986; Collins et al. 2002; Veatch 1906; Triska 1984) have resulted in significant changes to river morphology, the loss of aquatic biodiversity, and the degradation of riparian habitats (Graf 2001). To mitigate the negative effects of wood removal on ecosystems and geomorphology, the use of nature-based solutions (NBSs) is gaining popularity in river restoration projects owing to their ecological benefits and cost-effectiveness (Wohl et al. 2019; Shields and Nunnally 1984; USBR and ERDC 2016).

Both natural formations, such as large woody debris (LWDs), and engineered solutions, such as engineered log jams (ELJs), offer significant promise for river restoration. Illustrations of different types of NBSs can be found in the Supplemental Materials. A major advantage of ELJs and LWDs in river restoration practices is that they create diverse hydraulic conditions and deep scour pools, which are important for aquatic habitats (Abbe et al. 2003). ELJs, in particular, have great potential for river restoration because they are multifunctional. They provide both in-stream engineering benefits, such as stream stabilization (Suaznabar et al. 2021), as well as ecological benefits, such as restoring fish habitats (Brooks et al. 2006).

Background, Knowledge Gaps, and Objectives

A key characteristic of LWDs and ELJs is their porosity, leading to complex river responses compared to solid structures. Spreitzer et al. (2020a, b) researched large wood accumulations, employing structure-from-motion (SfM) photogrammetry, demonstrated the feasibility of quantifying porosity in NBSs comprising wooden materials. Their work, which focused on the characterization of accumulation shapes, sizes, and porosities, paves the way for future investigations into how these porosity characteristics influence the physics of flow and sediment transport. In the context of LWDs, Spreitzer et al. (2021) explored the impact of wood accumulations near piers on hydraulics and sediment transport patterns, providing insights into how spanwise large-wood accumulations influence river dynamics. In the application of ELJs that partially obstruct flow, Ismail et al. (2021) reported exploratory flume work on the effects of porosity on flow and sediment transport around ELJs. This paper reports further research with additional flume experiments to expand the parameter space and improve predictive formulas to better capture the distribution of porosity on the ELJ surface and within the whole volume.

Porous river restoration structures bear some resemblance to vegetation. Studies on turbulent flow in vegetation patches show the importance of porosity on the wake zone length scale and its dependence on the spacing of individual stems. The main cause of such dependence is the bleeding flow through pore spaces that affect the flow field, turbulence, shear stress, and consequently the bathymetry (Yagci et al. 2017; Follett and Nepf 2012; Kim et al. 2015; Waters and Curran 2016; Chen et al. 2012; Aberle and Järvelä 2013; Nepf 2012; Zong and Nepf 2012). Studies on vegetation are of paramount importance and have been extensively

[1]Ph.D. Candidate, Dept. of Civil and Environmental Engineering, Pennsylvania State Univ., University Park, PA 16802. Email: sfm5808@psu.edu

[2]Senior Hydraulic Engineer and Geomorphologist, Hydraulic Engineer Section, United States Army Corps of Engineers, Seattle, WA 98124. ORCID: https://orcid.org/0000-0002-4011-2803. Email: joanna.c.curran@usace.army.mil

[3]Associate Professor, Dept. of Civil and Environmental Engineering, Pennsylvania State Univ., University Park, PA 16802 (corresponding author). ORCID: https://orcid.org/0000-0002-8296-7076. Email: xzl123@psu.edu

Note. This manuscript was submitted on November 4, 2023; approved on October 15, 2024; published online on December 23, 2024. Discussion period open until May 23, 2025; separate discussions must be submitted for individual papers. This paper is part of the ***Journal of Hydraulic Engineering***, © ASCE, ISSN 0733-9429.

Table 1. Summary of literature on hydrodynamic and morphodynamic interactions with woody river restoration structures

Reference	Structure type	Phenomena investigated	Erodible bed	Porosity	$d_s = f(\underbrace{\text{porosity}, \ldots}_{\text{ourfocus}})$[a]	Scour time history
Wallerstein et al. (2001)	Partial and SW LWD	Drag and morphology	Yes	—	—	No
Gallisdorfer et al. (2014)	Partial side ELJs	Drag	Yes	$\phi_v \approx 0.68$ and 0.77	—	No
Bennett et al. (2015)	Partial side ELJ	Flow and drag	No	$\phi_v \approx 0.68$ and 0.77	—	No
Gallisdorfer et al. (2016)	Partial side ELJs	Morphology	Yes	$\phi_v \approx 0.68$ and 0.77	—	No
Schalko et al. (2019b)	SW LWD Accum.	Morphology	Yes	$\phi_v = 0.75$	$f(\phi_v, \ldots)$	No
Schalko et al. (2019a)	SW LWD Accum.	Backwater rise	Yes	$\phi_v = 0.75$	—	No
Schalko et al. (2021)	Single log	Flow	No	—	—	—
Muhawenimana et al. (2021)	SW leaky barrier	Backwater rise	No	$\phi_s = 0.4 - 0.8$ ($\phi_v = 0.25 - 0.75$)	—	No
Spreitzer et al. (2021)	SW LW Accum. at piers	Flow and morphology	Yes	$\phi_v = 0.65$	—	No
Schalko et al. (2021)	Single log	Flow	No	—	—	—
Ismail et al. (2021)	Side and center partial ELJs	Flow and morphology	Yes	$\phi_s = 0.29$ ($\phi_v = 0.72$)	$f(\phi_s, \ldots)$	No
Müller et al. (2021)	SW ELJ	Flow	No	$\phi_v = 0.41$ and 0.70	—	No
Müller et al. (2022)	SW ELJ	Flow	No	$\phi_v = 0.41 - 0.70$	—	No
This study	Side and center partial ELJ	Flow and morphology	Yes	$\phi_s = 0.15$ and 0.35 ($\phi_v = 0.45$ and 0.85)	$f(\phi_s, \phi_v, \ldots)$	Yes

Note: V_s = solid volume; ϕ_s = surface porosity; ϕ_v = volumetric porosity; Accum. = accumulation; SW = spanwise; and d_s = scour depth.
[a]Solid structures are not included in the porosity column.

researched, shedding light on sediment transport and flow dynamics around them. Ismail et al. (2021) highlighted the unique hydrodynamics around porous ELJs compared to cylinder array-like vegetation (Manners et al. 2007; Abbe and Brooks 2011). Thus, given the apparent differences in porosity distribution and geometry between vegetation and ELJs, findings from vegetation flow studies cannot be directly extrapolated to ELJs.

The scour of bed materials around in-stream structures plays an important role for creating deep pools and affecting the stability of in-stream structures (USBR and ERDC 2016). Hence, understanding the relationship between flow and sediment transport is essential for predicting river responses and ensuring the success of river restoration projects. An erodible bed will evolve as a result of sediment transport induced by the presence of these structures and flow alterations. Flow acceleration, deceleration, and turbulence can entrain or deposit sediment (Cherry and Beschta 1989; Abbe and Montgomery 1996; Dixon 2016; Daniels and Rhoads 2003). For instance, Kollmann et al. (1999) noted that LWDs accumulating on gravel bars significantly affect scour and deposition patterns, leading to the formation of pioneer islands.

This study builds upon previous work yet with very clear distinctions. A summary of representative hydraulics and sediment transport studies, focusing solely on the presence of large wood in-stream structures, is provided in Table 1. An extensive compilation of literature on the physical modeling of large wood (LW) through 2011 can also be found in Gallisdorfer et al. (2014). For instance, investigations have been carried out on the flow surrounding a single log (Schalko et al. 2021) or ELJs (Bennett et al. 2015) placed on a fixed bed. While studies on flow provide valuable insights, it is crucial to place ELJs on erodible beds to examine their morphological impact.

Other studies on wood barriers and porous piles show the importance of porosity in flow and sediment transport. The blockage ratio in channels, influenced by wood leaky barriers, significantly affects flood attenuation and backwater rise (Muhawenimana et al. 2021). A study on square hollow piles revealed that increased surface porosity reduced sediment transport and scour depth (Yang et al. 2021). Other research has taken a closer look at the morphodynamic aspects of LWDs. For example, Wallerstein et al. (2001) utilized a hydraulic model to assess the effects of LWDs on a sand bed, and Schalko et al. (2019b) examined the local scouring induced by spanwise LW accumulations. The latter research recommends a specific scour equation for scenarios involving spanwise LW accumulations like those found in fully blocked river cross sections. However, they did not recommend its use for situations of partial channel blockage, such as bridge pier scour. Consequently, their equation is not suitable for partial ELJ scenarios, as studied in this research.

ELJs, with their distinct geometric complexity characterized by large anchored key pieces and internally racked wood that partially obstructs flow, differ from vegetation and spanwise LWDs (Addy and Wilkinson 2016; Abbe 2006; Xu and Liu 2017; Manners et al. 2007; Abbe and Brooks 2011; Ismail et al. 2021). This is the main differentiation point between this work and most previous research.

Although the design of ELJs in this study is idealized, it holds real-world values. It aligns with the designs of apex ELJs, bar apex ELJs, and bank-attached deflector jam configurations, as evidenced by Abbe et al. (2018), Addy and Wilkinson (2016), Brooks et al. (2006), and Bennett et al. (2015). The ELJs utilized in this study are also similar to those applied in practical scenarios for fish habitats, such as fish hotels and Pennsylvania porcupine cribs (Norris et al. 2021; Clark-Kolaks 2015). Their design improves the habitat by offering hiding space for smaller fish from their predators, a feature

that distinguishes the ELJs in this study from LWDs with uniform porosity.

Currently, no comprehensive guidelines exists for assessing river responses to the introduction of ELJs, which can lead to uncertainties in engineering applications. Often, scour equations for nonporous piers or abutments are used when dealing with these porous structures. The effects of porosity are either only considered in the calculation of effective blockage area or not considered at all. Ismail et al. (2021) reported that the recommended equations in HEC-18 (Hydraulic Engineering Circular No. 18) for solid pier scour and in NCHRP 24-20 (National Cooperative Highway Research Program) for abutment scour under clear-water conditions (Arneson et al. 2012) are inadequate for estimating scour depths for porous structures.

The primary aim of this study is to further examine the turbulent flow unique to the presence of porous structures and to predict areas of sediment transport. We seek to identify areas of high turbulence, flow separation, and the wake regions with low velocity. The second focus is the sediment dynamics. Scour pattern and scour depth are analyzed. For practical purposes, an improved scour depth equation is proposed through a comprehensive parametric study. In ELJs, two types of porosity exist: volumetric porosity and surface or frontal porosity. We show that it is necessary to consider both surface and volumetric porosities. Existing scour depth formulas for solid structures are amended to include the effects of porosity. To address the reliance on specific idealized ELJ configurations and placements mentioned in this paper, we used data from other literature to develop a more generalized scour estimation method. The proposed formula is tested against a rare set of field measurement data on the South Fork of the Nooksack River, Washington, United States.

In this study, we performed flume experiments on porous ELJ structures within a clear-water scour regime. These structures were positioned either on the side or at the center of the flume. As presented in Table 1, there are limited studies on the impacts of porous ELJs on an erodible bed, considering both hydraulics and sediment transport. In this study, we examine ELJs, incorporating two distinct porosity values, thereby extending the scope of porosity ranges addressed in prior research with side and center placements. We delve deeper into the analysis, including maximum scour depth prediction and ELJs scour time history, which has no existing data in the context of ELJs. Moreover, for the first time, we consider the impact of both volumetric and surface porosities on scour depth.

The rest of the paper is structured as follows. The flume experiment details are introduced in the Methodology section. This is followed by presenting the results of mean flow velocity and turbulent kinetic energy. Afterward, the bathymetry findings are discussed. The discussion then extends to the relationship between bathymetry and flow features. Subsequent sections address the estimation of scour depth and its temporal evolution. Finally, the paper concludes by testing the proposed scour equation with field data.

Methodology

Laboratory Flume and Experiments

The experiments were conducted in a recirculating hydraulic flume with dimensions of 15.24 m long, 1.52 m wide, and 0.91 m deep (Fig. 1). The flume bottom was set to be close to horizontal ($S_0 = 0.00075$). The flume is equipped with a pump capable of generating a maximum flow rate of 240 L/s. A reservoir and a flow straightener are located upstream of the flume to guide the incoming flow to the test section. Side walls of the flume are made of glass for visualization. The flume is equipped with an instrument carriage that allows for horizontal, lateral, and vertical measurements.

The experiments were conducted using square column structures designed to mimic idealized ELJs. These experimental flume ELJs were constructed with a side length of 0.305 m. The ELJs were made from the stacks of wooden dowels with a diameter of 0.0254 m (Fig. 1). To fix the position of the testing structures, two wooden plates on the top and bottom of the stacked dowels and four vertical dowels at the four corners were used. The vertical dowels were 0.8 m long with a diameter of 0.0254 m. All ELJs were emergent and their height was greater than the flow depth. The x-axis is along the streamwise direction with $x = 0$ defined at the upstream edge of ELJs. The y-axis is along the spanwise direction and $y = 0$ is defined at the center of the flume.

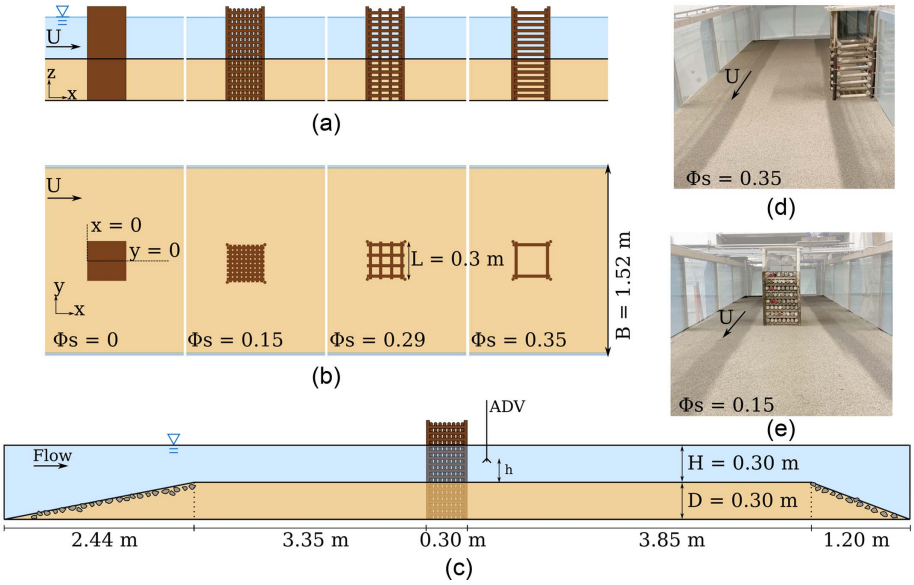

Fig. 1. Experiment setup and initial flume condition: (a) side view of different porosities; (b) plan view of different porosities; (c) flume setup; (d) side placement; and (e) center placement.

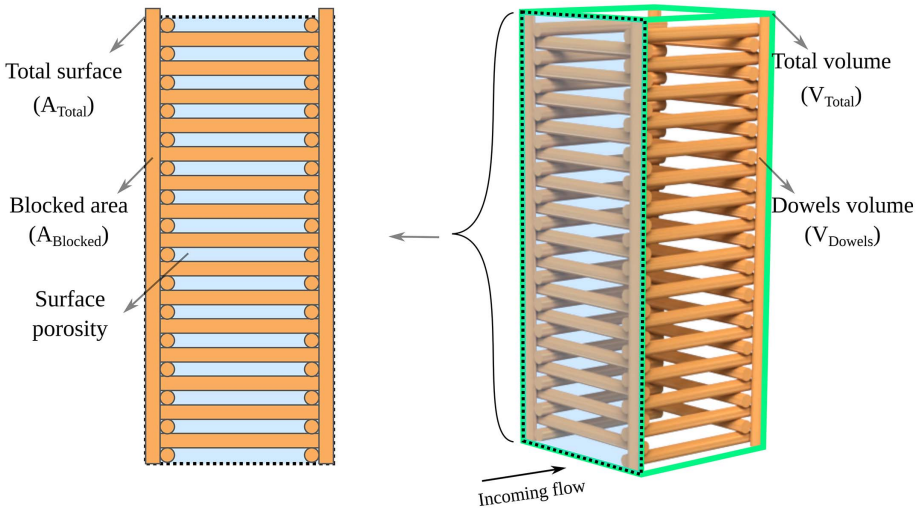

Fig. 2. Surface and bulk porosity definitions.

In the experiments, two different placements of ELJs were tested: along the wall (side) and in the middle of the flume (center). The volumetric porosity, ϕ_v, of ELJs was calculated as the ratio of void volume ($V_{\text{Total}} - V_{\text{Dowels}}$) to the total volume ($V_{\text{Total}}$). Here, V_{Dowels} is the volume of dowels. The surface porosity, ϕ_s, was calculated as the projected frontal porous area ($A_{\text{Total}} - A_{\text{Blocked}}$) to total frontal area (A_{Total}) of structures (Fig. 2). Here, A_{Blocked} is the frontal area blocked by dowels.

Building upon the work of Ismail et al. (2021), who reported four cases using the same flume and setup, this study conducted four additional tests with the ELJ's surface porosities at $\phi_s = 0.15$ and 0.35, across two placement locations (side and middle). Hence, we have conducted our analysis on a more comprehensive data set with surface porosities ϕ_s of 0 (solid), 0.15, 0.29, and 0.35, with their respective volumetric porosities (ϕ_v) of 0, 0.45, 0.72, and 0.85. According to Manners and Doyle (2008), the porosity estimates for wood jams, taking into account their evolution stages (material infilling) in river streams, vary between $\phi_v = 0.43$ and 0.88. Livers et al. (2020) have also assessed the volumetric porosity for field cases. They found it spans from 0.1 to 0.9 across various types of stream jams, ranging from small in-channel structures to large island apex formations.

The flume bed was covered with poorly graded medium sand. The sand depth is 0.305 m. The sediment geometric mean, D_g, is 0.94 mm and the gradation coefficient σ_g is 1.27. Cobblestone transition zones were placed upstream and downstream of the erodible bed to ensure a gradual transition from the rigid flume bed to the erodible bed. The structures were partially buried in the sand at a depth of 0.305 m from the rigid bed and located 3.35 m downstream of the transition section. The sand bed was extended to 3.85 m downstream of the ELJs to ensure that the dynamics of flow and sediment in the wake region was fully captured. Before each experiment, a scraper was used to level the sand bed and the flume was slowly filled with water to a depth of 0.305 m above the sand bed.

The flow discharge was designed such that scour around ELJs was in the clear-water scour regime, i.e., the background shear stress away from ELJs was smaller than the critical value. For the sediment used in this work, the target mean velocity and flow depth were set at $U = 0.26$ m/s and $H = 0.305$ m, respectively, with the control of variable speed pump. The real mean velocities for each experiment slightly deviated from the target value. The mean incoming velocities are determined at 25 points upstream of the structure, where the flow is fully developed and unaffected by the structure. Discharge for each cell around these points is computed by multiplying its velocity with its area. The average velocity is then derived by dividing the total discharge by the flume cross-sectional area for each experiment. The measured mean velocities with a Nortek Vectrino Plus acoustic Doppler velocimeter (ADV) and other test conditions of experiments are presented in Table 2. The Reynolds number and the Froude number for the target flow condition are $\mathsf{R}_D = UD/\nu = 7.9 \times 10^5$ and $\mathsf{F}_H = U/\sqrt{gH} = 0.15$, respectively. Here, D is the length scale of the ELJs' side length,

Table 2. Summary of test conditions of eight experiments

Case number	Case 1[a]	Case 2[a]	Case 3	Case 4	Case 5[a]	Case 6[a]	Case 7	Case 8
Structure type	Solid	Solid	Porous	Porous	Porous	Porous	Porous	Porous
Location	Side	Middle	Side	Middle	Side	Middle	Side	Middle
A_{Total} (m^2)	0.09	0.09	0.09	0.09	0.09	0.09	0.09	0.09
A_{Blocked} (m^2)	0.09	0.09	0.08	0.08	0.07	0.07	0.06	0.06
ϕ_s	0	0	0.15	0.15	0.29	0.29	0.35	0.35
ϕ_v	0	0	0.45	0.45	0.72	0.72	0.85	0.85
H	0.30	0.30	0.30	0.30	0.30	0.30	0.30	0.30
$U_{\text{ave,in}}$ (m/s)	0.25	0.26	0.26	0.25	0.26	0.27	0.26	0.25
Q_{in} (m^3/s)	0.11	0.12	0.12	0.17	0.12	0.12	0.12	0.12
F_H	0.14	0.15	0.15	0.14	0.15	0.15	0.15	0.14
R_d	75,335	80,215	79,605	76,250	79,300	81,740	78,995	76,250

[a]Ismail et al. (2021).

ν is the kinematic viscosity, and g is the gravitational acceleration. The mean velocity and the water depth for clear-water scour were determined through the combination of the Chezy equation and trial and error, such that the Shields number is less than the critical Shields number. The critical Shields number for the sand used is estimated to be $\theta_c = 0.0171$ (Brownlie 1981; Parker et al. 2003). The Shields number is defined by Shields (1936) as

$$\theta = \frac{u_*^2}{RgD_g} \tag{1}$$

where u_* is the shear velocity; R is the submerged specific gravity of sediment; and D_g is the grain size.

The inlet velocity profile along the vertical direction z was measured with the ADV in a cross section located at 1 m upstream of the ELJs. The profile was fitted to the log-law with the form of

$$\frac{u}{u_*} = 2.5 \ln\left(\frac{30z}{k_s}\right) \tag{2}$$

which provided the Nikuradse equivalent sand roughness, k_s, and the friction velocity, u_* (Roulund et al. 2005). To reduce the length of this paper, the fitted inlet velocity profile is shown in the Supplemental Materials. The fitted k_s has a value of 0.005 m and u_* has a value of 0.015 m/s; k_s is 5 times the value of D_{50}, which falls within the reasonable range of $ks = 1$ to 5 times D_{50} (or D_{65}, and D_{90}) as suggested by the literature (Sumer 2002; Camenen et al. 2009; Julien 2010). As a confirmation, the Shields parameter calculated with Eq. (1) has a value of $\theta = 0.015$, which is smaller than the critical value to ensure the clear-water scour regime.

Measurements and Data Processing

After the flume was filled with water to the desired depth, each test was then started by gradually increasing the flow to the targeted discharge. Local scour around ELJs started immediately. Depending on the porosity of ELJs, the time to reach scour equilibrium varied in a relatively wide range (45 to 125 h; see Table 2). In general, the increase of porosity in ELJs will increase the time to equilibrium.

Tests continued until the bed morphology reached a state of equilibrium, where no further significant changes were detected in the erodible bed. During the experiments, we periodically measured the maximum scour depths using a measuring tape affixed to the ELJ, aligning these measurements with the time elapsed since the experiment began. Furthermore, we employed photographs to document the exposed dowels to the flow (which were initially buried), enabling us to confirm the maximum scour depth and location at specific intervals. Upon reaching this scour equilibrium, velocity measurements were taken with an ADV both upstream and downstream of ELJs. These measurements capture the effects that changes in the erodible bed, such as scour and deposition. Data quality assurance was achieved by adjusting the ADV measurement properties. Based on recommendations from García et al. (2005), the signal-to-noise ratio was adjusted to be above 20 dB and the signal correlation was greater than 70%. Sampling frequency is defined as $F = f_a L/U_c$, where f_a is the sampling rate, and L and U_c are the integral length (flow depth) and velocity scales (free stream velocity), respectively. F was set to be greater than 20 in order to prevent errors associated with filtering. In order to satisfy the $F > 20$ requirement, a frequency of 40 Hz and a measurement duration of 60 s were used. The velocity raw data were postprocessed and despiked for analyzing the velocity and turbulence using techniques described in Goring and Nikora (2002). The time-averaged mean velocity and the fluctuating velocity components for each point measurement were calculated in the x-, y-, and z-directions, and the turbulent kinetic energy (TKE) was calculated as

$$\text{TKE} = k_t = 0.5(\overline{u'^2} + \overline{v'^2} + \overline{w'^2}) \tag{3}$$

where u', v', and w' are the deviations of velocity components from the respective means.

Velocity point measurements were made on four horizontal planes located at 0.02 m, 0.05 m, 0.08 m, and 0.15 m from the initial flat bed. The depths of these planes correspond to z/L values of 0.07, 0.16, 0.26, and 0.49, respectively. The horizontal range of the measurement section is defined as follows. In the streamwise direction, x/L is from -0.5 to 4 ($x/L = -0.5$ to 13 for Cases 3, 7 and 8). In the spanwise direction, y/L is from -1.5 to 1.5 for center placements and y/L is from 0.5 to 2.25 for side placements ($y/L = -0.25$ to 2.25 for Cases 7 and 8). Hence, for the middle placement cases, the velocity measurement grid extended L distance on both sides of ELJs. For side placement cases, the velocity measurement grid extended at least $2L$ distance into the middle of the flume. After the velocity measurement was completed, the pump was turned off and the flume was slowly drained. An Artec Eva 3D scanner was used to scan the final bathymetry.

Results and Analysis

Mean Flow Field

Explaining the morphological patterns around ELJs requires an understanding of the flow field. For solid structures such as bridge piers, the flow structure and scour are well understood. For example, the major flow features are the downward flow toward the bed in the upstream region, the horseshoe vortex around the structure, and the wake downstream. Subject to these flow features, sediment particles may be picked up and carried downstream, resulting in scour (Melville and Coleman 2000; Garcia 2008). With porosity, these major flow features are altered, which has implications for sediment transport. The schematic diagram of flow alteration around a porous ELJ compared to the solid model is shown in Fig. 3. In this section, detailed analysis is presented on the flow features.

Approaching Flow Deceleration

Contours of mean streamwise velocity on a horizontal plane at half water depth, $z = H/2$, are shown in Fig. 4. For all cases, the flow decelerates in the upstream region of the ELJ. The degree of deceleration depends on porosity and the placement of ELJs. To quantify, the streamwise and spanwise velocity profiles at $z = H/2$ are shown in Fig. 5. As porosity increases, the velocity deceleration upstream decreases. Flow deceleration also depends on the placement of ELJs in the flume. For instance, the flow deceleration upstream of ELJs is more pronounced for side placement cases compared to center placements. For the solid cases, at $x/L = -0.25$, the streamwise velocity in the upstream region drops to $0.75U$ and $0.5U$ for center and side placements, respectively. For porous structures, the upstream velocity decreases to $0.9U$ for center placement with $\phi_s = 0.29$ and $0.75U$ for side placement with $\phi_s = 0.35$. The difference in approaching flow deceleration stems from a higher stagnation pressure for solid cases and increased bleeding flow through highly porous ELJs.

Shear Layers

Shear layers form due to the velocity difference between the wake and the side regions of ELJs. The strength and extent of shear layers determine the turbulence and the capability of the flow to carry

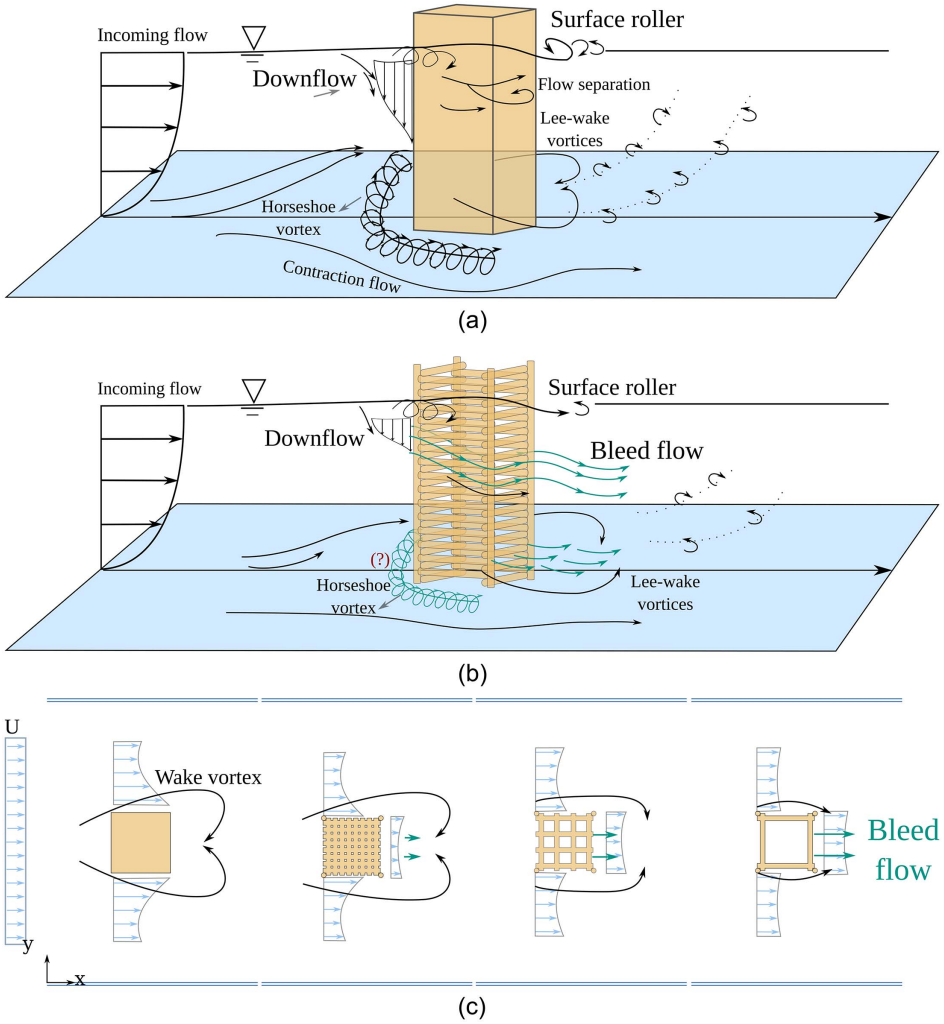

Fig. 3. Conceptual flow characteristics for (a) solid obstructions (adapted from Lai et al. 2022); (b) porous obstructions; and (c) plan view of flow around ELJs with different porosities.

sediment. The bleeding flow through porous ELJs reduces the strength of shear layers through two mechanisms. The first is the increase of downstream velocity in the wake area and thus smaller velocity difference. The second is the reduction in blockage effect. Part of the incoming flow passes directly through the porous structure and thus reduces the amount of flow going along the sides of ELJs. This essentially slows down the flow in the side regions of ELJs.

The increase of porosity decreases the strength of shear layers. For the solid cases, the flow separation and shear are more prominent than their porous counterparts. For porous cases, the shear layer is closer to the ELJ structures than the solid cases. This can be observed by the streamwise velocity contours in Fig. 4 and lateral velocity profiles in Figs. 5(b and c). For the solid, center placement case, the accelerated velocity contour line of $\bar{u}/U = 1.1$ begins at $y/L > 1$ and $0 < x/L < 2$. For comparison, for most porous ELJs, such as Case 8, this contour line starts at $x/L = 0.5$ and extends downstream instead of laterally. The spatial extent of the flow can be used to explain the spatial variation of the scour morphology, such as the width of the scour hole.

In reality, the porosity of ELJs may evolve with time. The porosity usually decreases as debris and small wood clog the ELJ interstitial space. The results in this work imply that the hydrodynamics and morphodynamics will evolve over time too. Newly installed ELJs with larger porosity will induce less flow obstruction and shear. However, old ELJs with decreased porosity will impart more flow obstruction, and much stronger shear layers should be observed. Understanding the dynamic evolution of the ELJ's porosity helps improve design and ecosystem service evaluation.

Wake and Recirculation Zone

Downstream of ELJs, wake vortices are a key feature that contribute to sediment transport. Within the wake zone, a recirculation zone may exist if the porosity is not high enough. A signature of a recirculation zone is the negative streamwise velocity, i.e., $\bar{u} < 0$. Fig. 4 shows that the area with negative streamwise velocity is larger in the solid cases than the porous cases. For ELJs placed in the center, the recirculation zone is closer to the solid structure and starts at $x/L = 2$ and continues to about $x/L = 3$ [Fig. 4(a)]. In contrast, for porous ELJs with $\phi_s = 0.15$, 0.29, and 0.35, the negative streamwise velocity is negligible, indicating the absence of a recirculation zone. However, downstream of porous ELJs, there exist wake zones characterized by a significantly reduced velocity magnitude. The same observations are made for ELJs placed along the side of the flume, which is shown in longitudinal velocity profiles in Fig. 5(c).

As depicted in Fig. 4, the wake and recirculation zone is more extensive for center placements compared to side placements.

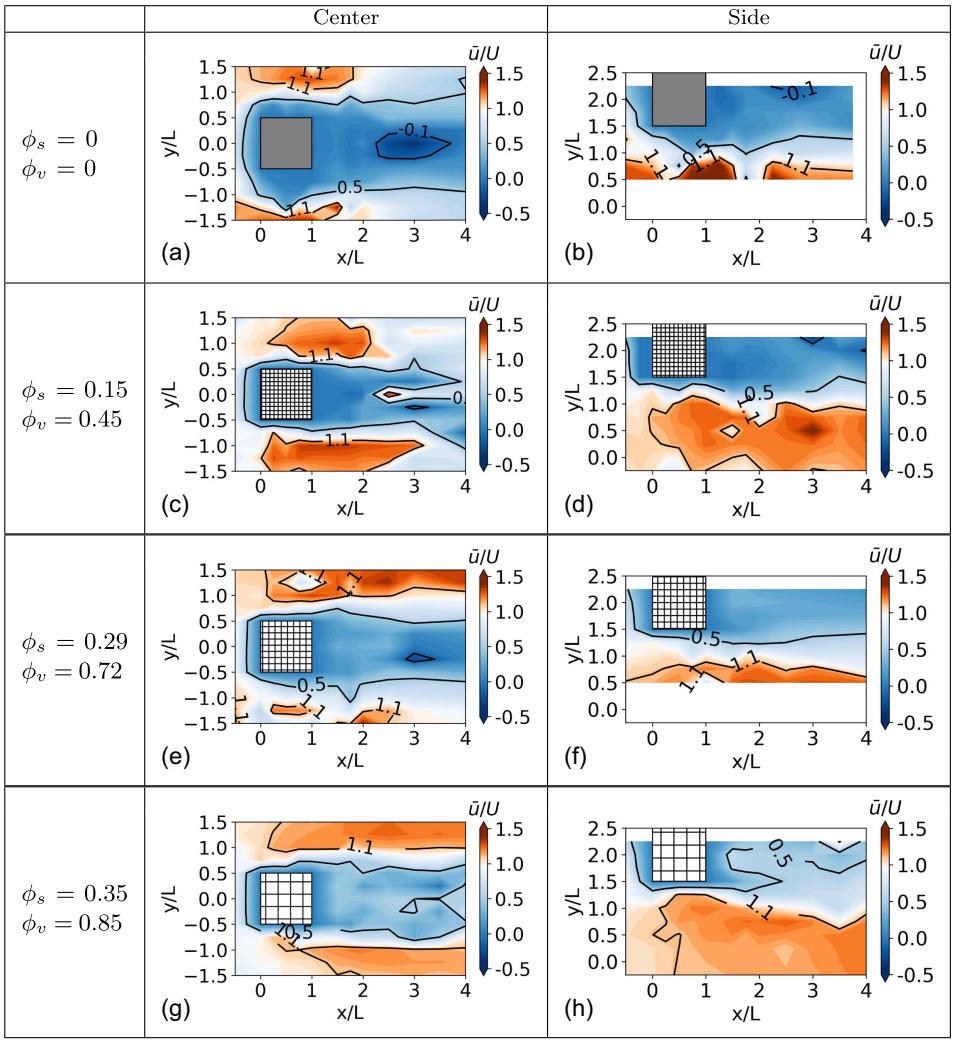

Fig. 4. Normalized streamwise velocity contour around ELJs. Plots in (a, b, e, and f) are generated using Ismail et al. (2021) data: (a) Case 2; (b) Case 1; (c) Case 4; (d) Case 3; (e) Case 6; (f) Case 5; (g) Case 8; and (h) Case 7.

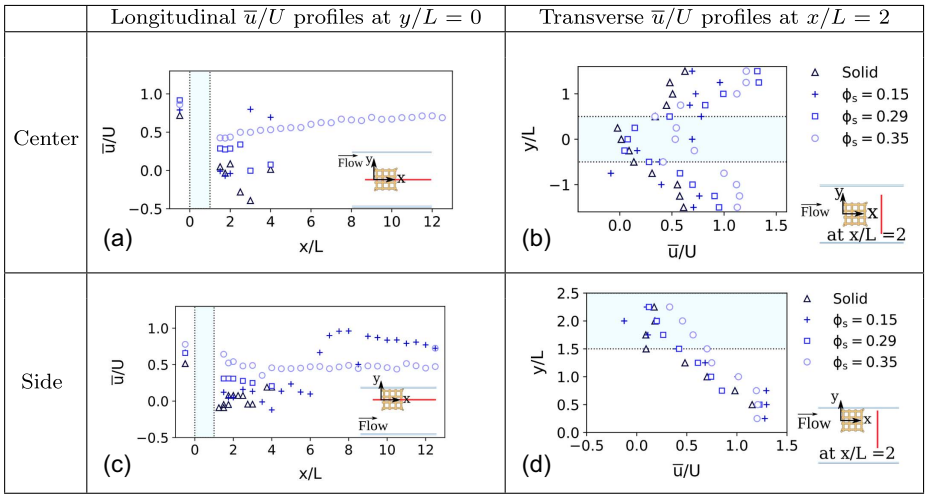

Fig. 5. Mean streamwise velocity profiles. Solid and $\phi_s = 0.29$. (Data from Ismail et al. 2021.)

For example, downstream of the side solid case, there is a negative velocity value of $\bar{u}/U = -0.1$, which is lower than the corresponding value of $\bar{u}/U = -0.4$ downstream of the center solid case.

In contrast to the solid cases, the velocity reduction in the wake zone for most porous ELJs placed in the center is low and nearly constant, which can be observed in the longitudinal velocity profiles in Fig. 5(a). Velocity variation in the longitudinal direction for the solid case continues to $x/L = 4$, which changes by about 50% from $x/L = 3.5$ to 4, whereas for the porous case with $\phi_s = 0.35$ the velocity change is less than 10%. Similarly, for ELJs placed along the side [Fig. 5(c)], for Case 3 with $\phi_s = 0.15$, the velocity variation continues to $x/L = 8$. For Case 7 with $\phi_s = 0.35$, the velocity is almost constant after $x/L > 4$.

Differences in the wake and recirculation zone can also be observed in the spanwise direction. Figs. 5(b and d) show the lateral profiles of the mean streamwise velocity at $x/L = 2$. The general trend in profiles for the solid and porous cases is similar. For porous cases, however, the profiles have more positive values because the bleeding flow through ELJs reduce or eliminate recirculation. The lateral extent of the wake, where there is a velocity reduction compared to the streamwise velocity, is greater for the solid cases than the porous cases. For ELJs placed at the center, the wake width is $y/L > 3$ for the solid case, $2 < y/L < 3$ for Case 4 ($\phi_s = 0.15$), $y/L < 2$ for Case 6 ($\phi_s = 0.29$), and $y/L < 1.5$ for Case 8 ($\phi_s = 0.35$). When ELJs are placed along the side, they are within the boundary layer of the flume's side way. Thus, a lower velocity reduction is observed in both lateral and longitudinal profiles. For the solid Case 1, the extent of lateral velocity reduction is at $y/L = 1.75$. For porous cases, the same extent is about $y/L = 1.5$. For the most porous ELJ (Case 7), velocity recovers to the approaching flow within a shorter distance from the trailing edge of the ELJs. The implication is that for more porous cases and side placement, the scour and deposition will be closer to ELJs and less drastic.

Turbulent Flow Field

Turbulence is investigated from the point of view of identifying the peak position and magnitude in this section. This will help us to understand how porous ELJs result in different bathymetric changes. TKE (k_t) contours are shown in Fig. 6. As porosity increases, turbulence in the wake of the ELJs decreases, and its peak position happens at further distances downstream. Peak k_t is about five times larger for the solid case than the porous case with $\phi_s = 0.35$. For ELJs at the center of flume, the x-coordinates of the $k_t = 0.5U^2$ contour line for the solid case is $x/l < 2$, while for the case of $\phi_s = 0.15$ it is $x/l > 2$. The same trend is true for two more porous ELJs. For example, the position of $k_t = 0.3U^2$ starts at $x/l = 2.75$ for $\phi_s = 0.29$, and $x/l = 3$ for $\phi_s = 0.35$. When compared to porous cases, the magnitude of peak k_t, as well as the area of higher k_t in the contours, are larger for solid cases. The same trend holds true for structures placed to the side; however, the highest k_t value is generally lower than center cases. For side ELJs, the $k_t = 0.5U^2$ contour line for the solid case is located at $x/L = 2.5$, while for $\phi_s = 0.15$ it is located at a larger distance ($x/L > 3$). For two more porous structures, Cases 5 and 7 with $\phi_s = 0.29$ and $\phi_s = 0.35$, respectively, the peak of the k_t contour line is about $0.1U^2$, which happens on the side and downstream of the ELJs (Fig. 6). For the TKE contours, it is also clear that the wake for side-placed ELJs is narrower than that for the center-placed ELJs.

Fig. 7 shows the longitudinal and transverse profiles of normalized TKE. The longitudinal profile of TKE shows that the peak for $\phi_s = 0.15$ occurs around $x/L = 4$, and $x/L = 2$ for $\phi_s = 0.35$. As the porosity decreases, the distance from the upstream edge of the ELJs to the peak turbulence increases. Shear layers and high TKE variations at the sides and downstream of the ELJs cause scouring to extend from upstream to downstream. Figs. 7(b and d) show the transverse profiles of TKE at $x/L = 2$. In general, these profiles have similar trends. TKE increases downstream in the wake and decreases outside. However, the magnitude and position of high and low values of TKE on the profiles depend on the porosity. In both center and side channel placements of ELJs, TKE magnitude decreases as porosity increases. This is because the bleeding flow suppresses the turbulence shear and TKE production.

Scour Hole Morphology

Porosity and structure placement have great influence on the equilibrium scour hole morphology. As an example, Fig. 8 shows photos of the equilibrium scour holes for two porosities of $\phi_s = 0.15$ and 0.35 ($\phi_v = 0.45$ and 0.85) and two placements (side and center). They correspond to Cases 3, 4, 7, and 8. The equilibrium bathymetries of all cases are shown in Fig. 9, where the scour and deposition are normalized by the length scale L of ELJs. The position of ELJs are shown with square patches. Qualitatively, Figs. 8 and 9 show that as porosity changes, scour and deposition differ drastically in both shape and magnitude. In general, solid cases exhibit more profound morphological changes than porous cases for both side and center placements of ELJs.

The scour hole morphology can be quantified by the maximum scour depth ($d_{s,\max}$), the height of the downstream bar (z_p), and the horizontal and lateral extents (l_s, l_p, and w_s; see Fig. 10 for their definitions) at the equilibrium. The maximum scour depth, observed on the upstream side of the structure at equilibrium, initially formed at the structure's upstream edge and gradually extended toward its middle during the experiment. The measured scour hole morphological metrics are listed in Table 3.

Scour hole size and depth decrease as porosity increases for both side and center placements of ELJs. For center-placed cases, the maximum scour depth is about $0.96L$ for the solid case ($\phi_s = 0$), $0.72L$ for Case 4 ($\phi_s = 0.15$), $0.68L$ for Case 6 ($\phi_s = 0.29$), and $0.5L$ for Case 8 ($\phi_s = 0.35$). Thus, the scour depth decreases substantially, almost by 50%, from the solid case to the most porous case. As discussed in the previous section, a shallower scour hole is consistent with the weaker flow deflection toward the bed in the upstream direction of ELJs (Fig. 5) caused by bleeding flow through logs and less stagnation.

The extent of scour in the spanwise direction, i.e., the width of scour hole (w_s), is about $4L$ for the solid case ($\phi_s = 0$), $3.8L$ for Case 4 ($\phi_s = 0.15$), $3L$ for Case 6 ($\phi_s = 0.29$), and $2.9L$ for Case 8 ($\phi_s = 0.35$). This is consistent with the shear layer and lateral velocity deflection analysis presented in the section "Shear Layers." Furthermore, with increasing porosity, the streamwise extents of the scour hole (l_s and l_p) decrease. For example, for the center-placed ELJ with $\phi_s = 0.15$, the longitudinal extent of scour l_s is about $4.1L$, while it is about $3L$ for $\phi_s = 0.35$. In contrast to the low-porosity ELJs [Figs. 9(a and c)], for higher-porosity cases with $\phi_s = 0.29$ and $\phi_s = 0.35$ [Figs. 9(e and h)], scour does not extend downstream as much, which can be observed in the experiment photos (Fig. 8).

As the porosity increases, the return flow intensity behind ELJs and wake extent decrease. Indeed, the return flow area is a good indicator for sediment deposition, as seen Fig. 9. The streamwise location of the deposition peak is closer to the ELJ and its scour hole as the porosity increases.

The porosity of ELJs also affected the scour and deposition shapes. For less porous ELJs, the scour hole downstream of the

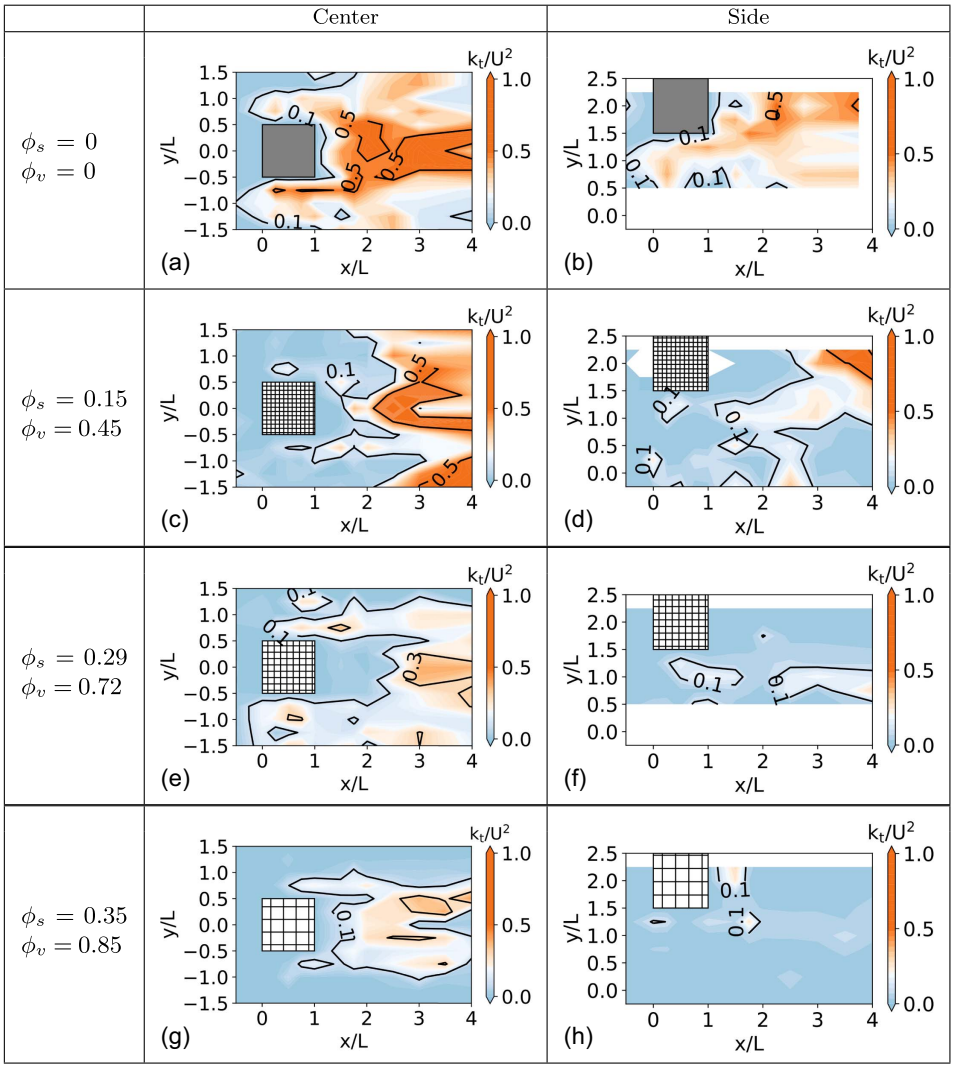

Fig. 6. Contour of normalized turbulent kinetic energy. Plots in (a, b, e, and f) are generated using Ismail et al. (2021) data: (a) Case 2; (b) Case 1; (c) Case 4; (d) Case 3; (e) Case 6; (f) Case 5; (g) Case 8; and (h) Case 7.

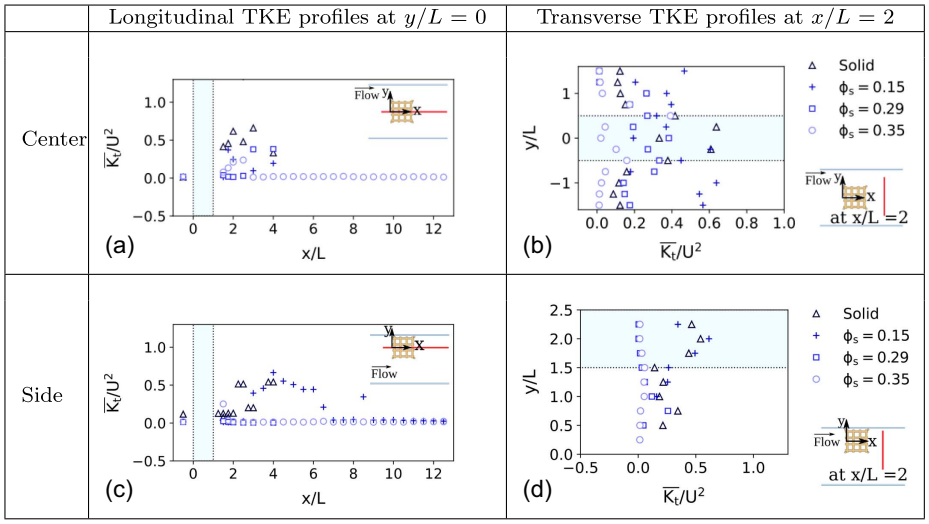

Fig. 7. Turbulent kinetic energy profiles in longitudinal and transverse directions. Solid and $\phi_s = 0.29$. (Data from Ismail et al. 2021.)

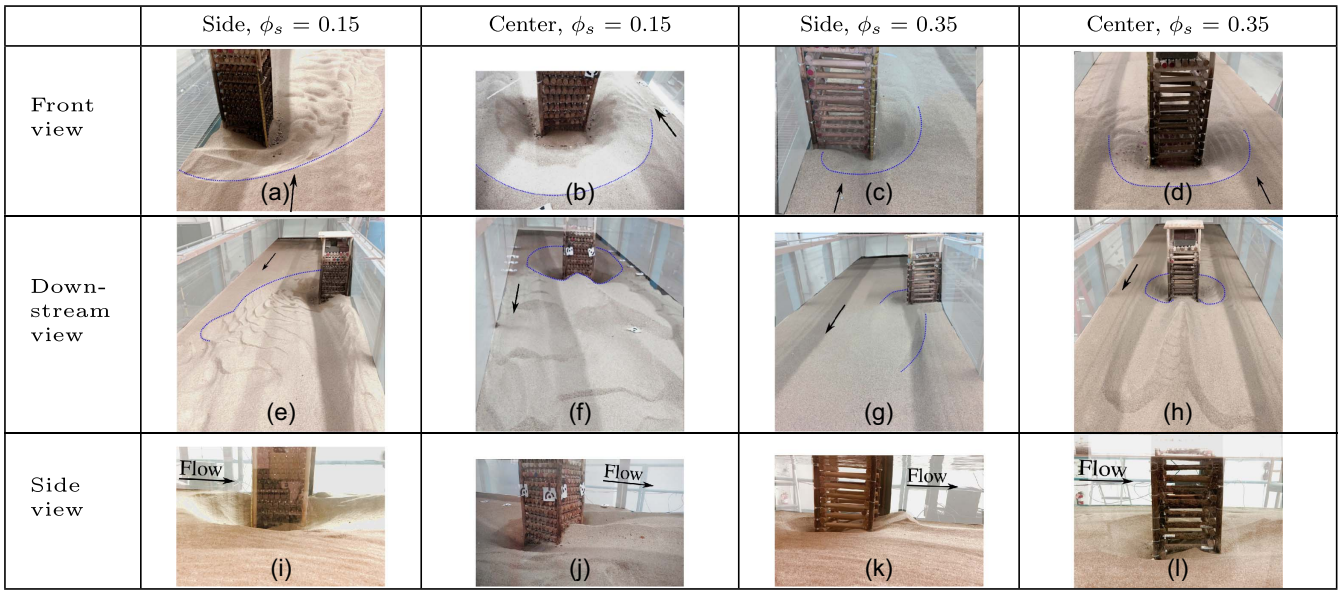

Fig. 8. Equilibrium scour features of (a, e, and i) Case 3; (b, f, and j) Case 4; (c, g, and k) Case 7; and (d, h, and l) Case 8. First row shows front view of ELJs, second shows the back view of the ELJs, and third row shows the side view of ELJs.

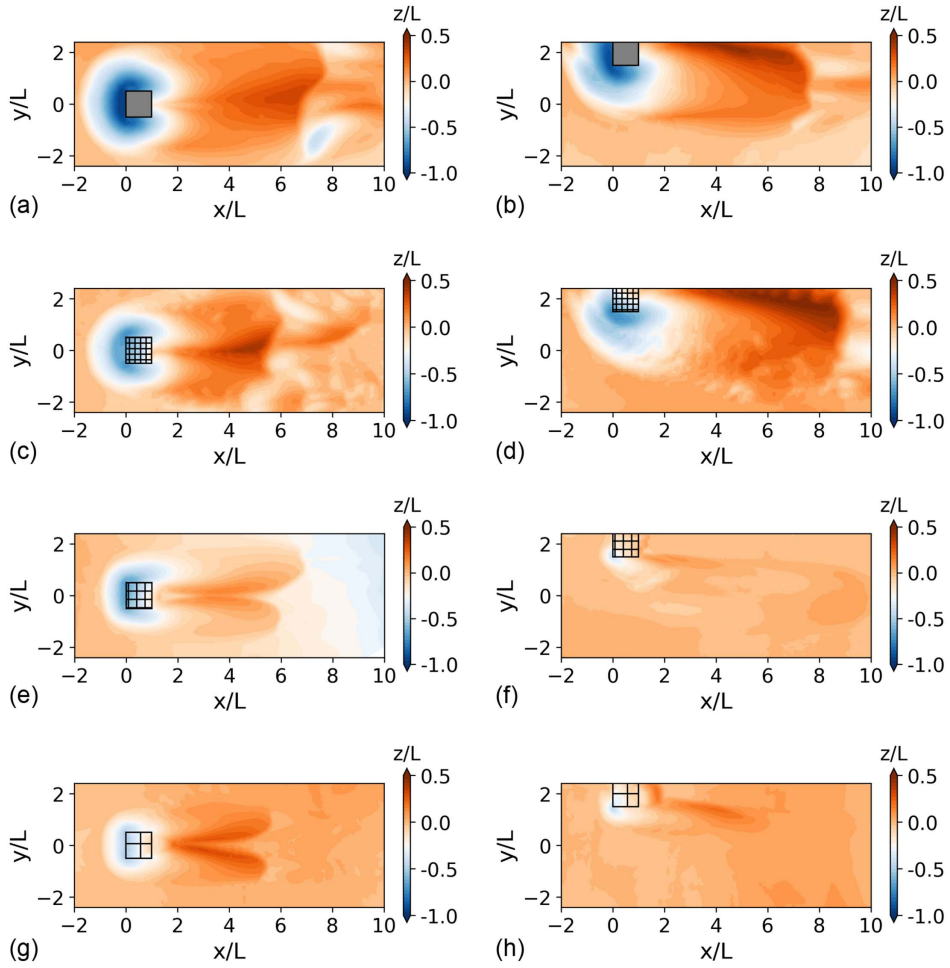

Fig. 9. Equilibrium bathymetry contours for all cases. Solid and $\phi_s = 0.29$: (a) Case 2: $\phi_s = 0$, $\phi_v = 0$; (b) Case 1: $\phi_s = 0$, $\phi_v = 0$; (c) Case 4: $\phi_s = 0.15$, $\phi_v = 0.45$; (d) Case 3: $\phi_s = 0.15$, $\phi_v = 0.45$; (e) Case 6: $\phi_s = 0.29$, $\phi_v = 0.72$; (f) Case 5: $\phi_s = 0.29$, $\phi_v = 0.72$; (g) Case 8: $\phi_s = 0.35$, $\phi_v = 0.85$; and (h) Case 7: $\phi_s = 0.35$, $\phi_v = 0.85$. (Data from Ismail et al. 2021.)

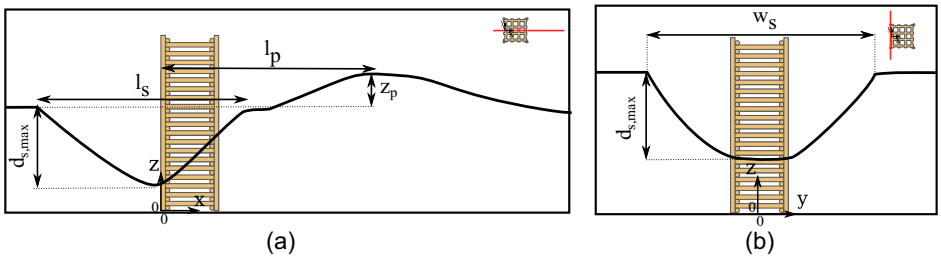

Fig. 10. Schematic diagram of bathymetric features: (a) longitudinal profile of bathymetry; and (b) lateral profile of bathymetry.

Table 3. Summary of test conditions and results for the eight experimental cases

Case no.	Case 1[a]	Case 2[a]	Case 3	Case 4	Case 5[a]	Case 6[a]	Case 7	Case 8
Structure	Solid	Solid	Porous	Porous	Porous	Porous	Porous	Porous
Location	Side	Middle	Side	Middle	Side	Middle	Side	Middle
ϕ_s	0	0	0.15	0.15	0.29	0.29	0.35	0.35
ϕ_v	0	0	0.45	0.45	0.72	0.72	0.85	0.85
$d_{s,\max}/L$	0.92	0.96	0.76	0.72	0.42	0.68	0.4	0.5
l_s/L	>5	>5	5.2	4.1	2.5	4	3.3	3
w_s/L	4	3	3.5	3.8	2.5	3	2	2.9
z_p/L	0.33	0.35	0.56	0.42	0.1	0.12	0.06	0.3
l_p/L	6.81	6.34	7.17	4.88	2.19	3.90	1.73	3

[a]Ismail et al. (2021).

structure converged to the centerline and formed a horseshoe shape [Figs. 9(a and c)]. This was not observed in the study of Follett and Nepf (2012) for solid and dense circular vegetation patches. The results suggest that the scour hole morphology is affected by the shape of the structures (square versus circular).

For the center placement of ELJs, the solid case and the case with $\phi_s = 0.15$ have similar morphological patterns, where the deposition bar resembles a triangular wedge. For the cases with $\phi_s = 0.29$ and $\phi_s = 0.35$, the deposition bar consists of two elongated hills separated by an open triangular region in which neither erosion nor deposition have taken place. The difference between the two groups is caused by whether the flow in the wake has enough strength to push sediment toward the middle.

Comparing the bathymetry of side-placement cases with center-placement cases, it is clear that the patterns are similar. If the side wall serves as a mirror, the morphological pattern of the side-placement cases is half of those for center-placement cases. In addition, the magnitudes of scour depth and deposition are also comparable.

Overlapping of Flow and Bathymetric Features

The location and magnitude of significant bathymetric features correspond well with the flow features, such as the flow structure, velocity, and TKE (see Figs. 4 and 6). For example, for Case 3 with $\phi_s = 0.15$ and a side placement, the lowest velocity and highest TKE happen at about $x = 4L$, after which the velocity and TKE recover back to the incoming flow condition at about $x = 7L$. This corresponds well with the depositional footprint from $4L$ to $7L$ in Fig. 9(c). For Case 5 with a center placement, the lowest velocity and the highest TKE are from about $2L$ to $3L$, which is also consistent with the peak deposition that happens at about $2.19L$ (see Fig. 9 and Table 3). A similar observation can be made for the spanwise extent of bed morphology, which again shows the strong correlation between flow and bathymetric features.

The depositional bar downstream is directly related to the wake and recirculation zone behind ELJs. Comparing the mean flow field shown in the section "Shear Layers" and the bathymetry contours in Fig. 9, it is clear that the recirculation zones have almost the same footprint as the depositional bars for all cases. It is also found that as porosity increases, the correlation among the width of wake and shear layer and bathymetric changes weakens. Nevertheless, the deposition peak occurred at the lowest reduced velocity and the highest TKE downstream. The spatial distribution of velocity and turbulence contains valuable information for sediment movement around ELJs.

Scour Depth Prediction

We propose a new formula for porosity correction for scour depth prediction that involves both surface and volumetric porosities. Ismail et al. (2021) proposed a simple linear correction to the clear-water scour formula in HEC-18 and the correction is a linear function of the ELJ's surface porosity. However, with the extended data set from this work and the literature, we found it is beneficial to include the effect of volumetric porosity. The reason is that ELJs have different designs in practice and wood members are not evenly distributed within the structures. In a scenario where an ELJ lacks internal wood or materials, its surface porosity serves as the control for passing and blocking flow. In general, surface porosity, ϕ_s, can be interpreted as a gate through which incoming flow enters the porous structures. On the other hand, the volumetric porosity, ϕ_v, characterizes the bulk behavior of passing fluid and momentum extraction. Thus, it is the combination of both porosities that determines the overall flow and sediment transport around ELJs.

A scour depth correction coefficient due to porosity is defined as

$$s_c = \frac{d_{p,s}}{d_{s,s}} = f(\phi_s, \phi_v) \tag{4}$$

where $d_{p,s}$ is the scour depth of a porous structure. $d_{s,s}$ is the scour depth of the corresponding solid structure, which is calculated with

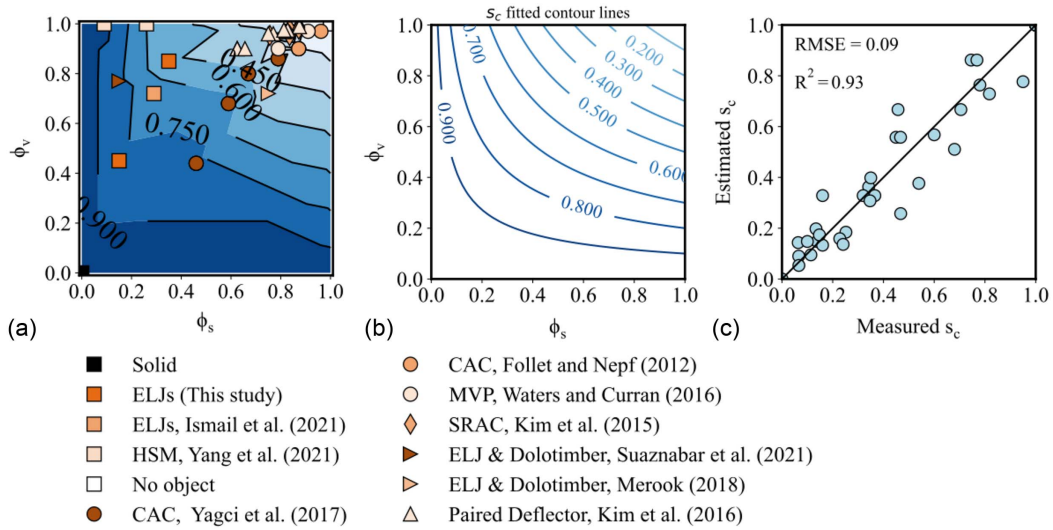

Fig. 11. (a) Contour of scour depth correction coefficient s_c. Data are compiled from different sources. ELJs = engineered log jams, CAC = circular array of cylinder, MVP = model vegetation patches, SHM = hollow square monopile, and SRAC = side rectangular array of cylinders. (b) Contour of proposed scour depth correction coefficient $s_c = 1 - \phi_s^{0.62}\phi_v^{1.00}$. (c) Comparison between measured and predicted scour depth correction coefficients.

empirical scour depth equations under clear-water conditions recommended in HEC-18 for center-placement cases and in the NCHRP 24-20 Report of abutment scour for side-placement cases (Arneson et al. 2012).

Our goal is the functional form for the scour depth correction coefficient $s_c = f(\phi_s, \phi_v)$. Our proposed functional form is based on the observed trend from the experimental data and a simple asymptotic analysis. Fig. 11(a) shows the contour plot of s_c as a function of both ϕ_s and ϕ_v. Here, s_c was calculated based on Eq. (4). The contour plot includes not only data from this work but also data for various other porous structures/features in the literature. The extra data include the finite patch of cylinders mimicking aquatic vegetation patches (Yagci et al. 2017; Follett and Nepf 2012; Kim et al. 2015; Waters and Curran 2016), porous monopiles (Yang et al. 2021), ELJs and dolotimber structures (Ismail et al. 2021; Merook 2018; Suaznabar et al. 2021), and porous paired deflectors (Kim et al. 2016). All these cases share the same porous nature. While we recognize the geometric differences between our square ELJ and in-stream structures from the existing literature, we have adapted our equivalent solid scour depth calculations to suit each specific scenario. Consequently, differences arising from geometry differences are not contributing to the prediction of scour coefficient. This approach also accommodates varying erodible bed materials, further standardizing our findings across different scenarios.

In Fig. 11(a), to plot the contour of s_c, the asymptotic values for $\phi_s = 0$ (the vertical axis) and $\phi_v = 0$ (the horizontal axis) were also used. When $\phi_s = 0$ or $\phi_v = 0$, either the surface or the whole volume is impervious. Thus, the structure acts like a solid and s_c should have a value of 1.0. At the origin where both ϕ_s and ϕ_v have a value of 0, the structure is a solid (both inside and out), and s_c has a value of 1.0. The other asymptotic behavior is as ϕ_s and ϕ_v both approach 1.0, i.e., toward the upper-right corner point, the whole porous structure disappears (no solid) and s_c should have a value of 0. Along the diagonal line from the origin to the upper-right corner point, the porosity inside and out is uniform, i.e., $\phi_s = \phi_v$, and the porosity correction coefficient s_c gradually transitions from 1 to 0. Ismail et al. (2021) used a linear function for this transition.

The contour lines in Fig. 11(a) are L-shaped with significant nonlinearity near the origin and gradually become linear close to the upper-right corner. This behavior can be described by a production function of ϕ_s and ϕ_v as

$$s_c = 1 - a\phi_s^b\phi_v^c \tag{5}$$

This functional form satisfies the asymptotic behaviors described above for $\phi_s = 0$ and $\phi_v = 0$. A nonlinear least-squares method was used to fit the data and find the coefficient in Eq. (5). Since at the upper-right corner point $\phi_s = \phi_v = 1$, and $s_c = 0$, a has to be 1. Setting $a = 1$, curve fitting resulted in the values $b = 0.62$ and $c = 1.0$.

For comparison, the contours of the fitted function in Eq. (5) are plotted in Fig. 11(b). It can be observed that the fitted equation captures the trend shown in Fig. 11(a). In practice, Eq. (5) can be directly used to estimate the porosity correction coefficient for porous structures.

Our new porosity correction coefficient in Eq. (5) improves the predictive performance in comparison with the simple linear correction proposed in Ismail et al. (2021), which has the form of

$$s_c = 1 - \phi \tag{6}$$

where ϕ is the overall porosity. In this formula, it is assumed that the surface and volumetric porosities are the same, i.e., $\phi = \phi_s = \phi_v$. With this assumption, our new formula in Eq. (5) can be simplified as

$$s_c = 1 - a\phi^{b+c} = 1 - \phi^{1.62} \tag{7}$$

It is clear that the major difference between the two is the power to the porosity ϕ. Our new data suggested a nonlinear power law instead of a linear law. The new formula is also more general because it can consider the disparity in surface and volumetric porosities. The better performance can be appreciated in Fig. 11(c), where the measured s_c of all data points and estimated s_c using our new formula are plotted together. The root-mean-square error (RMSE) is 0.09 and the R^2 has a high value of 0.93.

Temporal Scaling Analysis of Scour

The temporal evolution of the scour hole around ELJs is also of great importance to the design and evaluation of such in-stream structures. Using a similar approach as described in Song et al. (2022), we conduct a simple scaling analysis and introduce a novel function to describe the evolution of scour depth. Previously, temporal scour evolution has also been studied by Melville and Chiew (1999), Oliveto and Hager (2002), and Yang et al. (2020) for bridge piers. A comparison with and appraisal of Melville and Chiew (1999) will be provided.

The scour depth $d_s(t)$ can be made dimensionless with the maximum scour depth $d_{s,\max}$, where t denotes time. The dimensionless scour depth can be written as a functional relationship as follows:

$$\frac{\mathrm{d}_s(t)}{\mathrm{d}_{s,\max}} = f\left(\frac{u_*}{u_{*c}}, \frac{H}{L}, \frac{L}{d}, \frac{t}{t_e} \text{ or } \frac{t}{t_0}, \phi_v, \phi_s\right) \tag{8}$$

where u^* is the bed shear velocity; u_{*c} is the critical bed shear velocity; d is sediment diameter; L is the object length scale; t_0 is the baseline timescale; and t_e is the equilibrium timescale for scour. Let sediment size be D, then since $L/D > 50$, the effect of bed sediment can be neglected (Melville and Coleman 2000). The effect of porosity (ϕ_v and ϕ_s) is already embedded in the maximum scour depth $d_{s,\max}$. All other parameters are the same for all cases and known except the timescale, t_0.

According to Song et al. (2022), the baseline timescale can be calculated as $t_0 = L^2/q$. In which q is the bedload transport and L is the length scale of the object. There are many empirical bedload transport formulas. In this work, the one proposed in Engelund and Fredsøe (1976) was used:

$$\frac{q}{\sqrt{RgD^3}} = 18.74(\theta - \theta_c)(\theta^{1/2} - 0.7\theta_c^{1/2}) \tag{9}$$

where the submerged specific gravity of sediment is $R = (s-1) = 1.65$ for the sand used. q is the bed-load transport, which is dependent on applied shear velocity u_* through $\theta = (u_*^2)/(RgD)$. The applied shear velocity due to contraction velocity along sides of porous ELJs is calculated to estimate the bed-load transport. Here, the contraction flow is the main scour driver. Contraction velocity itself depends on the surface porosity (ϕ_s), blockage of the structures $(1-\phi_s)L$, and width of flume (b), which can be calculated as $U_{\text{contraction}} = [Ub]/[b-(1-\phi_s)L)]$. Knowing the contraction velocity, the applied shear velocity can be estimated as (Song et al. 2022; Chen et al. 2019):

$$\frac{U_{\text{contraction}}}{u_*} = 5.75\log\left(\frac{12.2H}{k_s}\right) \tag{10}$$

With θ_c previously calculated as 0.0171 in the Methodology section and the contraction θ already determined, q can now be calculated. The value of t_0 for ϕ_s values of 0.35 and 0.15 are 0.60 h and 0.50 h, respectively. Fig. 12 shows the nondimensionalized scour depth of ELJs with surface porosity of $\phi_s = 0.15$ and $\phi_s = 0.35$ of side and center placement plotted versus the dimensionless time, t/t_0.

The scour data of all four cases in this study are then fitted to the saturation growth curve in Eq. (11). Fig. 12 displays the fitted equation, where the value of a represents the normalized scour depth at equilibrium, which is $s_c = a = 1.02$. When the dimensionless time is equal to b, the normalized scour depth will be half of the equilibrium value, or $s_c = 0.5$ at $t/t_0 = b = 29.49$. The fitted line in Fig. 12(a) closely matches the measurement data

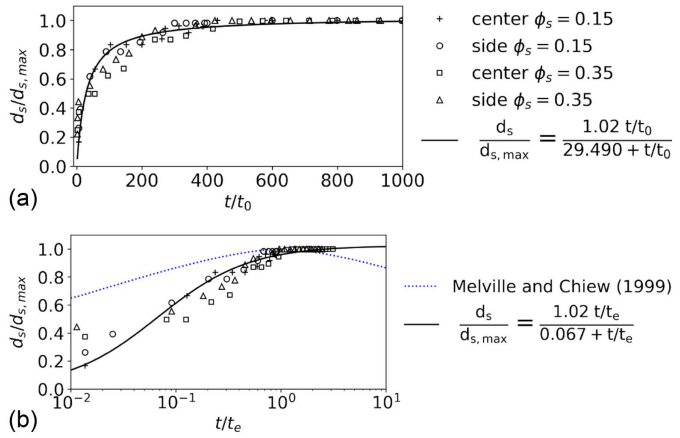

Fig. 12. Temporal development of normalized scour depth and saturation growth curve fitted line.

$$\frac{\mathrm{d}_s}{\mathrm{d}_{s,\max}} = \frac{at/t_0}{b + t/t_0} \tag{11}$$

To demonstrate the significance of using our proposed formula to estimate the temporal evolution of scour depth in porous structures, we compared it to the formula presented by Melville and Chiew (1999) for solid circular piers. To ensure the comparability of our timescale with the Melville and Chiew (1999) formula, the equilibrium timescale was estimated using Eq. (11). In calculating the equilibrium timescale, it is assumed that the scour depth is 95% of the maximum scour depth $d_{s,\max}$. By substituting the scour depth ratio and the fitted coefficients a and b, the equilibrium time, t_e, for ELJs with porosity (ϕ_s) values of 0.35 and 0.15 are calculated as 263.89 h and 220.33 h, respectively. Following a similar methodology as in a previous analysis, we normalized the scour depth data and time, this time with respect to the equilibrium time t_e, and fitted them to a saturation growth curve. The obtained results are presented in Fig. 12(b). Our findings suggest that our proposed formula is more suitable for accurately predicting the scour depth of porous squared ELJs, while the equations designed for solid structures fail to provide an accurate estimate for these structures. Additionally, our proposed formula provides a more accurate prediction of the initial scour depth than the equation proposed by Melville and Chiew (1999). Moreover, the equation proposed by Melville and Chiew (1999) has a limitation that it is not applicable for times greater than the equilibrium timescale, and it predicts decreasing scour depth for large time values, which is physically unrealistic.

Real-World Case Demonstration

The results of the previous sections are based on small-scale experiments. To ensure relevance and applicability at the field scale, a "reality check" with real-world data is essential. In this section, we test the proposed scour equation in the previous section with a real-world case.

The field site is located on the South Fork Nooksack River in the Cascades Range in Washington State. Over the course of several years, bathymetric and flow data have been collected at this site. In the 2000s, ELJs were constructed to direct flow into side and chute channels to increase overall channel complexity and salmon spawning opportunities. Around these structures, significant morphological changes have been observed and measured since the installation of ELJs in this reach. SfM and acoustic surveys were

Table 4. Summary of the field ELJ case

Variables	Values
Flow rate Q (m^3/s)	35.34
Water depth H (m)	0.6
D_{50} (m)	0.02
ELJ position	Side
ELJ length D (m)	9.1
ELJ width L (m)	3.7
ϕ_s	0.33
ϕ_v	0.47
$d_{p,s}$ (m)	1.9
$d_{s,s}$ (NCHRP 24-20) (m)	2.51
Measured s_c	0.76
Estimated s_c	0.75

combined to measure the detailed topography and underwater bathymetry of the restoration site.

Table 4 provides the detailed hydraulics, sediment, and ELJ data. A hydraulic data measurement of channel flow from field measurements in 2018 is used to estimate the scour coefficient here. For that measurement, the upstream flow rate was 35.34 m^3/s and the upstream flow depth was 0.6 m. According to the sediment size distributions, D_{50} is about 20 mm. At ELJ #8, the maximum flow depth was 2.5 m. This resulted in a maximum measured scour depth of 1.9 m in the upstream side of the ELJ.

ELJ #8 extends 3.7 m into the channel and its length along the channel is 9.1 m. On the left bank of the main channel, ELJ #8 was constructed using 40 logs (see Supplemental Materials). For the construction of ELJs, about 30 m^3 of smaller wood pieces (slash) were used to fill the voids of the structure, which was about 30% of the total volume. According to the preliminary design documents of the ELJ #8 (Nooksack Indian Tribe 2015), the surface and volumetric porosities are calculated (Table 4). In the design of the ELJ #8 some of the logs had rootwad. In the calculation of porosity, we simplified these logs to cylindrical logs without rootwad. Using the equations in NCHRP 24-20 for abutment scour under clear-water conditions (Arneson et al. 2012), the solid scour depth is calculated as 2.5 m. Hence, using Eq. (4), the scour depth coefficient is 0.76, which is consistent with the estimated scour depth coefficient of 0.75 using Eq. (5).

Discussion

This study focuses on ELJs that partially obstruct flow, with minimal impact on water surface levels, in contrast to full-channel spanning LWDs that were the focus of numerous previous studies (Table 1).

Our tests reveal that flow features around in-stream structures are crucial for understanding the extent of scour and the locations of peak deposition through the analysis of shear layers, lateral velocity deflection, and peak TKE areas. By collecting data at the equilibrium state of an erodible bed, we account for new types of vortices occurring within the scour hole or resulting from the deposition bars, which lead to further sediment removal. This work offers insights into equilibrium flow dynamics not addressed in previous studies on flat bed (Table 1).

Comparing the bathymetric features of ELJs with those from vegetation patch studies reveals different scour patterns. Thus, finding a generalized solution for predicting physical features such as scour for various shapes of porous structures presents a challenge. A key observation is that ELJs and other porous structures with identical volumetric porosities may not exhibit the same surface porosities, and vice versa. Typically, patches of cylindrical dowels, as documented in the literature, display surface porosities greater than 0.5, positioning them closer to the right corner of the $\phi_v - \phi_s$ graph (refer to Fig. 11). In contrast, ELJs are located on the left side of $\phi_s = 0.5$, with a spectrum of volumetric porosities.

Our analysis emphasizes the importance of both surface and volumetric porosities in influencing flow interaction and structure behavior, revealing a nonlinear relationship between porosity and scour depth. This observation challenges current recommendations (USBR and ERDC 2016) for predicting scour around ELJs, which typically overestimate scour depth by not accounting for porosity.

There are some limitations in the current research. Our analysis assumes constant porosity, which may not always reflect reality. In the real world, porosity may decrease due to material accumulation in scenarios of high wood supply and transport. The volumetric porosities in our experiments ranged from 0.45 to 0.85. Research by Manners and Doyle (2008) suggests that porosity estimates for wood jams vary between 0.43 and 0.88 during their evolutionary stages in river streams, confirming the relevance of our selected values in the field.

More research should be conducted to investigate the effects of changing porosity on flow and scour. Manners and Doyle (2008) showed that changes in porosity within naturally formed jams vary with the stages of jam formation. Initially, the stabilization of a key piece does not significantly alter porosity. For example, the jams studied by Wallerstein et al. (2001) fall into this initial stage. Manners et al. (2007) reported that a jam filled with small gravels and branches will not become completely full but will instead achieve a stable porosity, which is the case for fully accumulated jams. Manners and Doyle (2008) further observed that once a jam reaches a stable porosity value, the flow is diverted around the jam, leading to only minor changes in porosity and volume.

Our ELJs, already stabilized with key members, may attract medium-sized or smaller materials, thus altering the porosity based on their initial state. The flow contraction and diversion around Cases 1 to 4 resulted in ELJs with the lowest porosity values, exhibiting behavior similar to natural jams with complete accumulation or older ELJs. Conversely, Cases 5 to 8, characterized by higher bleeding flow through the structure and lower flow contraction, exhibit similarities with natural jams that are partially formed. They are comparable to newly installed ELJs with larger porosity that contain only key logs and may lead to further debris accumulation. For the field case application discussed in this paper, the ELJ serves as an example of a fully accumulated jam, as it was initially filled with small materials such as twigs and gravel. Furthermore, considering that the timescale of porosity changes substantially exceeds that of bathymetric changes, it is reasonable to consider the initially designed porosity as stable and the primary factor influencing bathymetry.

Given the insights from the discussion and acknowledging porosity as a dynamic variable, we recommend that researchers and practitioners apply the proposed correction factor for a minimum scour depth estimate and use existing guidelines for solid structures for a maximum scour estimate. This approach enables informed decisions by providing a range of scour depth for planning and design.

Conclusions

This study examines flow and morphological features around porous ELJs that partially obstruct flow. The bleeding flow through porous ELJs results in reduced contraction velocity and turbulence production. As a result of these flow alterations, bathymetric

features around highly porous ELJs become less prominent. Scour is reduced and more localized to the structure. Porosity also influences the shape of bathymetric features. Depending on the porosity, the reattachment of shear layers downstream of structures can cause the scour to elongate downstream, extending through the centerline of the flow or toward the side wall of the channel. Consequently, the depositional bar in the wake of ELJs may take the shape of either an open or closed triangular wedge. This comparative analysis of surface and volumetric porosities of ELJs, alongside morphological features, provides insights for erodible bed alteration in river restoration and NBS applications.

Current guidelines for predicting scour depth around the NBS are based on principles designed for solid structures and often overpredict scour depth due to neglecting porosity. This study conducted experiments and analyzed structures with a wide range of porosities, leading to an improved scour depth prediction. A scour depth correction coefficient, derived from experimental data and literature, adjusts for surface and volumetric porosities through regression analysis. This new formula significantly improves the prediction accuracy over previous methods, and its applicability has been confirmed with a field case. Therefore, for practical applications, the findings of this research emphasize the importance of calculating and collecting both surface and volumetric porosity of an in-stream NBS for river restoration. Additionally, a simple scale analysis captures the temporal evolution of scour, aiding in understanding the flow-ELJ-sediment system dynamics.

Data Availability Statement

All data that support the findings of this study are available from the corresponding author upon reasonable request.

Acknowledgments

This work was supported by the National Science Foundation (Award #1935243).

Supplemental Materials

There are supplemental materials associated with this paper online in the ASCE Library (www.ascelibrary.org).

References

Abbe, T. 2006. *Conceptual design guidelines: Application of engineered logjams*. Rep. for the Scottish Environmental Protection Agency. Seattle: Herrera Environmental Consultants.

Abbe, T., and A. Brooks. 2011. "Geomorphic, engineering, and ecological considerations when using wood in river restoration." In Vol. 194 of *Stream restoration in dynamic fluvial systems: Scientific approaches, analyses, and tools*, 419–451. Washington, DC: American Geophysical Union.

Abbe, T., M. Hrachovec, and S. Winter. 2018. "Engineered log jams: Recent developments in their design and placement, with examples from the pacific northwest, USA." In *Reference module in earth systems and environmental sciences*. Amsterdam, Netherlands: Elsevier. https://doi.org/10.1016/B978-0-12-409548-9.11031-0.

Abbe, T., G. Pess, D. R. Montgomery, and K. L. Fetherston. 2003. "Integrating engineered log jam technology into river rehabilitation." Chap. 17 in *Restoration of Puget sound rivers*, 443–482. Seattle: University of Washington Press.

Abbe, T. B., and D. R. Montgomery. 1996. "Large woody debris jams, channel hydraulics and habitat formation in large rivers." *Regul. Rivers: Res. Manage.* 12 (2–3): 201–221. https://doi.org/10.1002/(SICI)1099-1646(199603)12:2/3<201::AID-RRR390>3.0.CO;2-A.

Aberle, J., and J. Järvelä. 2013. "Flow resistance of emergent rigid and flexible floodplain vegetation." *J. Hydraul. Res.* 51 (1): 33–45. https://doi.org/10.1080/00221686.2012.754795.

Addy, S., and M. Wilkinson. 2016. "An assessment of engineered log jam structures in response to a flood event in an upland gravel-bed river." *Earth Surf. Processes Landforms* 41 (12): 1658–1670. https://doi.org/10.1002/esp.3936.

Arneson, L. A., L. W. Zevenbergen, P. F. Lagasse, and P. E. Clopper. 2012. *Evaluating scour at bridges*. Rep. No. FHWA-HIF-12-003. Vienna, VA: National Highway Institute.

Bennett, S. J., S. M. Ghaneeizad, M. S. Gallisdorfer, D. Cai, J. F. Atkinson, A. Simon, and E. J. Langendoen. 2015. "Flow, turbulence, and drag associated with engineered log jams in a fixed-bed experimental channel." *Geomorphology* 248 (Nov): 172–184. https://doi.org/10.1016/j.geomorph.2015.07.046.

Bernhardt, E. S., et al. 2005. "Synthesizing US river restoration efforts." *Science* 308 (5722): 636–637. https://doi.org/10.1126/science.1109769.

Brooks, A. P., T. Abbe, T. Cohen, N. Marsh, S. Mika, A. Boulton, T. Broderick, D. Borg, and I. Rutherfurd. 2006. *Design guideline for the reintroduction of wood into Australian streams*. Canberra, ACT, Australia: Land & Water Australia.

Brownlie, W. R. 1981. *Prediction of flow depth and sediment discharge in open channels*. Rep. No. KH-R-43A. Pasadena, CA: W. M. Keck Laboratory of Hydraulics and Water Resources, California Institute of Technology.

Camenen, B., M. Larson, and A. Bayram. 2009. "Equivalent roughness height for plane bed under oscillatory flow." *Estuarine Coastal Shelf Sci.* 81 (3): 409–422. https://doi.org/10.1016/j.ecss.2008.11.019.

Chen, Y., R. A. DiBiase, N. McCarroll, and X. Liu. 2019. "Quantifying flow resistance in mountain streams using computational fluid dynamics modeling over structure-from-motion photogrammetry-derived microtopography." *Earth Surf. Processes Landforms* 44 (10): 1973–1987. https://doi.org/10.1002/esp.4624.

Chen, Z., A. Ortiz, L. Zong, and H. Nepf. 2012. "The wake structure behind a porous obstruction and its implications for deposition near a finite patch of emergent vegetation." *Water Resour. Res.* 48 (9): W09517. https://doi.org/10.1029/2012WR012224.

Cherry, J., and R. Beschta. 1989. "Coarse woody debris and channel morphology: A flume study 1." *JAWRA J. Am. Water Resour. Assoc.* 25 (5): 1031–1036. https://doi.org/10.1111/j.1752-1688.1989.tb05417.x.

Clark-Kolaks, S. 2015. *Aquatic habitat enhancement plan for the placement of natural and artificial habitats in Indiana's reservoirs*. Indianapolis: Indiana Dept. of Natural Resources.

Collins, B. D., D. R. Montgomery, and A. D. Haas. 2002. "Historical changes in the distribution and functions of large wood in Puget lowland rivers." *Can. J. Fish. Aquat.Sci.* 59 (1): 66–76. https://doi.org/10.1139/f01-199.

Daniels, M. D., and B. L. Rhoads. 2003. "Influence of a large woody debris obstruction on three-dimensional flow structure in a meander bend." *Geomorphology* 51 (1–3): 159–173. https://doi.org/10.1016/S0169-555X(02)00334-3.

Dixon, S. J. 2016. "A dimensionless statistical analysis of logjam form and process." *Ecohydrology* 9 (6): 1117–1129. https://doi.org/10.1002/eco.1710.

Engelund, F., and J. Fredsøe. 1976. "A sediment transport model for straight alluvial channels." *Hydrol. Res.* 7 (5): 293–306. https://doi.org/10.2166/nh.1976.0019.

Follett, E. M., and H. M. Nepf. 2012. "Sediment patterns near a model patch of reedy emergent vegetation." *Geomorphology* 179 (Dec): 141–151. https://doi.org/10.1016/j.geomorph.2012.08.006.

Gallisdorfer, M. S., S. J. Bennett, J. F. Atkinson, S. M. Ghaneeizad, A. P. Brooks, A. Simon, and E. J. Langendoen. 2014. "Physical-scale model designs for engineered log jams in rivers." *J. Hydro-Environ. Res.* 8 (2): 115–128. https://doi.org/10.1016/j.jher.2013.10.002.

Gallisdorfer, M. S., S. J. Bennett, S. M. Ghaneeizad, and J. F. Atkinson. 2016. "Morphodynamic responses of physical-scale experimental river

channels to engineered logjams for stream restoration design." In *River flow*, 2354–2359. London: CRC Press.
Garcia, M. 2008. *Sedimentation engineering: Processes, measurements, modeling, and practice*. 1st ed. Reston, VA: ASCE. https://doi.org/10.1061/9780784408148.
García, C. M., M. I. Cantero, Y. Niño, and M. H. García. 2005. "Turbulence measurements with acoustic Doppler velocimeters." *J. Hydraul. Eng.* 131 (12): 1062–1073. https://doi.org/10.1061/(ASCE)0733-9429(2005)131:12(1062).
Goring, D. G., and V. I. Nikora. 2002. "Despiking acoustic Doppler velocimeter data." *J. Hydraul. Eng.* 128 (1): 117–126. https://doi.org/10.1061/(ASCE)0733-9429(2002)128:1(117).
Graf, W. L. 2001. "Dam age control: Restoring the physical integrity of America's rivers." *Ann. Assoc. Am. Geogr.* 91 (1): 1–27. https://doi.org/10.1111/0004-5608.00231.
Harmon, M. E., et al. 1986. "Ecology of coarse woody debris in temperate ecosystems." *Adv. Ecol. Res.* 15 (Jan): 133–302. https://doi.org/10.1016/S0065-2504(08)60121-X.
Ismail, H., Y. Xu, and X. Liu. 2021. "Flow and scour around idealized porous engineered log jam structures." *J. Hydraul. Eng.* 147 (1): 04020089. https://doi.org/10.1061/(ASCE)HY.1943-7900.0001833.
Julien, P. Y. 2010. *Erosion and sedimentation*. Cambridge, UK: Cambridge University Press.
Kim, H. S., I. Kimura, and Y. Shimizu. 2015. "Bed morphological changes around a finite patch of vegetation." *Earth Surf. Processes Landforms* 40 (3): 375–388. https://doi.org/10.1002/esp.3639.
Kim, H. S., I. Kimura, and Y. Shimizu. 2016. "Experimental investigations of scour pools around porous obstructions." *Water* 8 (11): 498. https://doi.org/10.3390/w8110498.
Kollmann, J., M. Vieli, P. Edwards, K. Tockner, and J. Ward. 1999. "Interactions between vegetation development and island formation in the alpine river Tagliamento." *Appl. Veg. Sci.* 2 (1): 25–36. https://doi.org/10.2307/1478878.
Lai, Y. G., X. Liu, F. A. Bombardelli, and Y. Song. 2022. "Three-dimensional numerical modeling of local scour: A state-of-the-art review and perspective." *J. Hydraul. Eng.* 148 (11): 03122002. https://doi.org/10.1061/(ASCE)HY.1943-7900.0002019.
Livers, B., K. B. Lininger, N. Kramer, and A. Sendrowski. 2020. "Porosity problems: Comparing and reviewing methods for estimating porosity and volume of wood jams in the field." *Earth Surf. Processes Landforms* 45 (13): 3336–3353. https://doi.org/10.1002/esp.4969.
Manners, R., and M. Doyle. 2008. "A mechanistic model of woody debris jam evolution and its application to wood-based restoration and management." *River Res. Appl.* 24 (8): 1104–1123. https://doi.org/10.1002/rra.1108.
Manners, R. B., M. Doyle, and M. Small. 2007. "Structure and hydraulics of natural woody debris jams." *Water Resour. Res.* 43 (6): W06432. https://doi.org/10.1029/2006WR004910.
Melville, B. W., and Y.-M. Chiew. 1999. "Time scale for local scour at bridge piers." *J. Hydraul. Eng.* 125 (1): 59–65. https://doi.org/10.1061/(ASCE)0733-9429(1999)125:1(59).
Melville, B. W., and S. E. Coleman. 2000. *Bridge scour*. Littleton, CO: Water Resources.
Merook, A. T. 2018. "Laboratory assessment of scour evolution around engineered logjams in gravel bed rivers." M.S. thesis, Dept. of Civil and Environmental Engineering, Univ. of Tennessee.
Muhawenimana, V., C. A. Wilson, J. Nefjodova, and J. Cable. 2021. "Flood attenuation hydraulics of channel-spanning leaky barriers." *J. Hydrol.* 596 (May): 125731. https://doi.org/10.1016/j.jhydrol.2020.125731.
Müller, S., E. Follett, P. Ouro, and C. Wilson. 2022. "Influence of channel-spanning engineered logjam structures on channel hydrodynamics." *Water Resour. Res.* 58 (12): e2022WR032111. https://doi.org/10.1029/2022WR032111.
Müller, S., C. A. Wilson, P. Ouro, and J. Cable. 2021. "Experimental investigation of physical leaky barrier design implications on juvenile rainbow trout (*Oncorhynchus mykiss*) movement." *Water Resour. Res.* 57 (8): e2021WR030111. https://doi.org/10.1029/2021WR030111.
Nepf, H. M. 2012. "Flow and transport in regions with aquatic vegetation." *Annu. Rev. Fluid Mech.* 44 (1): 123–142. https://doi.org/10.1146/annurev-fluid-120710-101048.
Nooksack Indian Tribe. 2015. "South Fork Nooksack Hutchinson reach restoration phase 1." Accessed July 16, 2022. https://srp.rco.wa.gov/project/360/17268.
Norris, A., M. Hutchison, D. Nixon, J. Shiau, and A. Kaus. 2021. *Fish attractors in impoundment fisheries: A best practice guideline*. Project Rep. Queensland, Australia: State of Queensland.
Oliveto, G., and W. H. Hager. 2002. "Temporal evolution of clear-water pier and abutment scour." *J. Hydraul. Eng.* 128 (9): 811–820. https://doi.org/10.1061/(ASCE)0733-9429(2002)128:9(811).
Parker, G., C. M. Toro-Escobar, M. Ramey, and S. Beck. 2003. "Effect of floodwater extraction on mountain stream morphology." *J. Hydraul. Eng.* 129 (11): 885–895. https://doi.org/10.1061/(ASCE)0733-9429(2003)129:11(885).
Roulund, A., B. M. Sumer, J. Fredsøe, and J. Michelsen. 2005. "Numerical and experimental investigation of flow and scour around a circular pile." *J. Fluid Mech.* 534 (Jul): 351–401. https://doi.org/10.1017/S0022112005004507.
Schalko, I., C. Lageder, L. Schmocker, V. Weitbrecht, and R. M. Boes. 2019a. "Laboratory flume experiments on the formation of spanwise large wood accumulations: I. Effect on backwater rise." *Water Resour. Res.* 55 (6): 4854–4870. https://doi.org/10.1029/2018WR024649.
Schalko, I., C. Lageder, L. Schmocker, V. Weitbrecht, and R. M. Boes. 2019b. "Laboratory flume experiments on the formation of spanwise large wood accumulations: Part II—Effect on local scour." *Water Resour. Res.* 55 (6): 4871–4885. https://doi.org/10.1029/2019WR024789.
Schalko, I., E. Wohl, and H. M. Nepf. 2021. "Flow and wake characteristics associated with large wood to inform river restoration." *Sci. Rep.* 11 (1): 1–12. https://doi.org/10.1038/s41598-021-87892-7.
Shields, A. 1936. "Anwendung der aehnlichkeitsmechanik und der turbulenzforschung auf die geschiebebewegung." Ph.D. thesis, Preussischen Versuchsanstalt für Wasserbau, Technical Univ.
Shields, F. D., Jr., and N. R. Nunnally. 1984. "Environmental aspects of clearing and snagging." *J. Environ. Eng.* 110 (1): 152–165. https://doi.org/10.1061/(ASCE)0733-9372(1984)110:1(152).
Song, Y., S. A. M. Darzikolaei, and X. Liu. 2022. "Scour around underwater unexploded ordnances (UXOs): An experimental and computational investigation." *Ocean Eng.* 258 (Oct): 112146. https://doi.org/10.1016/j.oceaneng.2022.112146.
Spreitzer, G., J. Tunnicliffe, and H. Friedrich. 2020a. "Large wood (LW) 3D accumulation mapping and assessment using structure from motion photogrammetry in the laboratory." *J. Hydrol.* 581 (Feb): 124430. https://doi.org/10.1016/j.jhydrol.2019.124430.
Spreitzer, G., J. Tunnicliffe, and H. Friedrich. 2020b. "Porosity and volume assessments of large wood (LW) accumulations." *Geomorphology* 358 (Jun): 107122. https://doi.org/10.1016/j.geomorph.2020.107122.
Spreitzer, G., J. Tunnicliffe, and H. Friedrich. 2021. "Effects of large wood (LW) blockage on bedload connectivity in the presence of a hydraulic structure." *Ecol. Eng.* 161 (Mar): 106156. https://doi.org/10.1016/j.ecoleng.2021.106156.
Suaznabar, O., Z. Xie, R. T. Kilgore, S. Leon, D. Pastrich, C. Zuelow, C. Huang, and K. Kerenyi. 2021. *Applying engineered logjams and dolosse for streambank stabilization*. Rep. No. FHWA-HRT-21-028. Washington, DC: US Federal Highway Administration, Office of Infrastructure Research and Development.
Sumer, B. M. 2002. *The mechanics of scour in the marine environment*. Singapore: World Scientific.
Triska, F. J. 1984. "Role of wood debris in modifying channel geomorphology and riparian areas of a large lowland river under pristine conditions: A historical case study." *Int. Ver. Theor. Angew. Limnol.: Verhandlungen* 22 (3): 1876–1892. https://doi.org/10.1080/03680770.1983.11897589.
USBR and ERDC (Bureau of Reclamation and US Army Engineer Research and Development Center). 2016. *National large wood manual: Assessment, planning, design, and maintenance of large wood in fluvial ecosystems: Restoring process, function, and structure*. Washington, DC: USBR and ERDC.
Veatch, A. C. 1906. *Geology and underground water resources of northern Louisiana and southern Arkansas*. Washington, DC: US Government Printing Office.

Vitousek, P. M., H. A. Mooney, J. Lubchenco, and J. M. Melillo. 1997. "Human domination of earth's ecosystems." *Science* 277 (5325): 494–499. https://doi.org/10.1126/science.277.5325.494.

Wallerstein, N. P., C. V. Alonso, S. J. Bennett, and C. R. Thorne. 2001. "Distorted Froude-scaled flume analysis of large woody debris." *Earth Surf. Processes Landforms* 26 (12): 1265–1283. https://doi.org/10.1002/esp.271.

Waters, K. A., and J. C. Curran. 2016. "Effects of an emergent vegetation patch on channel reach bathymetry and stability during repeated unsteady flows." *Water Resour. Res.* 52 (11): 9066–9085. https://doi.org/10.1002/2015WR018411.

Wohl, E., et al. 2019. "The natural wood regime in rivers." *Bioscience* 69 (4): 259–273. https://doi.org/10.1093/biosci/biz013.

Xu, Y., and X. Liu. 2017. "Effects of different in-stream structure representations in computational fluid dynamics models—Taking engineered log jams (ELJ) as an example." *Water* 9 (2): 110. https://doi.org/10.3390/w9020110.

Yagci, O., I. Yildirim, M. F. Celik, V. Kitsikoudis, Z. Duran, and V. O. Kirca. 2017. "Clear water scour around a finite array of cylinders." *Appl. Ocean Res.* 68 (Oct): 114–129. https://doi.org/10.1016/j.apor.2017.08.014.

Yang, F., L. Qu, G. Tang, and L. Lu. 2021. "Local scour around a porous surface-piercing square monopile in steady current." *Ocean Eng.* 223 (Mar): 108716. https://doi.org/10.1016/j.oceaneng.2021.108716.

Yang, Y., B. W. Melville, G. H. Macky, and A. Y. Shamseldin. 2020. "Temporal evolution of clear-water local scour at aligned and skewed complex bridge piers." *J. Hydraul. Eng.* 146 (4): 04020026. https://doi.org/10.1061/(ASCE)HY.1943-7900.0001732.

Zong, L., and H. Nepf. 2012. "Vortex development behind a finite porous obstruction in a channel." *J. Fluid Mech.* 691 (Jan): 368–391. https://doi.org/10.1017/jfm.2011.479.